Erschienen in: Soft Matter ; 12 (2016), 41. - S. 8485-8494
https://dx.doi.org/10.1039/c6sm01376g

Soft Matter

PAPER

View Article Online
View Journal | View Issue

Cite this: Soft Matter, 2016, 12, 8485

A combined 3D and 2D light scattering study on aqueous colloidal model systems with tunable interactions

Yi Liu,[a] Nathalie Claes,[b] Bastian Trepka,[c] Sara Bals[b] and Peter R. Lang*[ad]

Received 16th June 2016,
Accepted 22nd August 2016

DOI: 10.1039/c6sm01376g

www.rsc.org/softmatter

In this article we report on the synthesis and characterization of a system of colloidal spheres suspended in an aqueous solvent which can be refractive index-matched, thus allowing for investigations of the particle near-wall dynamics by evanescent wave dynamic light scattering at concentrations up to the isotropic to ordered transition and beyond. The particles are synthesized by copolymerization of a fluorinated acrylic ester monomer with a polyethylene-glycol (PEG) oligomer by surfactant free emulsion polymerization. Static and dynamic light scattering experiments in combination with cryo transmission electron microscopy reveal that the particles have a core shell structure with a significant enrichment of the PEG chains on the particles surface. In index-matching DMSO/water suspensions the particles arrange in an ordered phase at volume fraction above 7%, if no additional electrolyte is present. The near-wall dynamics at low volume fraction are quantitatively described by the combination of electrostatic repulsion and hydrodynamic interaction between the particles and the wall. At volume fractions close to the isotropic to ordered transition, the near-wall dynamics are more complex and qualitatively reminiscent of the behaviour which was observed in hard sphere suspensions at high concentrations.

1 Introduction

The properties of colloidal particles at or close to interfaces between an aqueous and a non-aqueous phase have acquired growing attention from the scientific community and industry during recent years.[1] The spectrum of topics spans fundamental scientific subjects such as particle stabilized emulsions,[2] protein stability and adsorption[3] or self-assembly at water–oil interfaces[4] for the fabrication of functional nano-films, with industrial applications such as corrosion protection[5] or water-borne 'green' coatings,[6] to name a few examples. While there is a plethora of publications considering static properties such as interaction forces, structure formation and phase behaviour of particles at interfaces,[7–9] there are comparatively few contributions reporting on experimental investigations of particle dynamics in the ultimate vicinity of interfaces,[10–18] despite the fact that the dynamics of colloidal particles at interfaces is an important feature, especially when the dimension of confining geometries are approaching those of the particles, as in the case of microfluidics,[19] emulsion stabilization[20,21] as well as many biological processes.[22,23] Interfaces between a solid and a liquid phase are of particular technological importance *e.g.* in coating processes or bio-film formation. In these cases, the motion of the particles close to the wall is slowed down due to hydrodynamic interaction and this hindrance differs for particles moving parallel and perpendicular to the wall.[24,25] The interplay between static particle wall interaction and the slowing-down caused by the so-called wall drag effect has significant implications in potential applications. Geometrical constraints were used to quench Brownian rotational motion of spherical Janus particles providing a means to steer their trajectory.[26] Furthermore, the trajectories of active swimmers, driven by flagellar motion, can be directed by tuning their interaction with a surface, and spatial confinements can be used to accumulate active swimmers.[27] For a targeted exploitation of the combined effects of static interaction, the wall drag effect and particle concentration, a fundamental understanding of their mutual interplay is essential. In this paper we report on the synthesis and characterization of an aqueous system, which allows a systematic variation of the static interactions and at the same time enables the study of the near-wall dynamics of particles at arbitrary concentrations.

For experimental purposes, interfaces between transparent solids and a liquid phase are convenient, since in this case, the near-wall dynamics of colloidal particles can be investigated by evanescent wave dynamic light scattering (EWDLS). This technique

[a] Forschugszentrum Jülich, Institute of Complex Systems ICS-3, Jülich, Germany. E-mail: p.lang@fz-juelich.de
[b] Electron Microscopy for Materials Research (EMAT), University of Antwerp, Belgium
[c] University of Konstanz, Germany
[d] Heinrich-Heine Universität, Düsseldorf, Germany

was first devised by Lan *et al.* in 1986,[28] and has been advanced constantly since then. The principle is as follows: an evanescent wave is created as an illumination source when a laser beam is totally reflected off a glass–solution interface; particles, which are located within this illumination profile will scatter light, which is then collected by a detecting unit and passed down to a correlator to generate the intensity correlation function. The penetration depth of the evanescent wave can be tuned by varying the incident angle of the laser beam. Being a light scattering technique in essence, EWDLS is most suited to the measurement of particles within a radius range around 100 nm, and at the same time provides good statistics. Modern instrumentation has made it possible to independently vary the scattering vector components parallel, $Q_{\parallel}$, and normal, $Q_{\perp}$, to the interface and hence to distinguish between the anisotropic diffusivity of colloids parallel and perpendicular to the interface experimentally.[15] EWDLS has also been employed to study the rotational diffusion of optically anisotropic particles,[29] to probe the particle dynamics at liquid–liquid interfaces,[30] and to measure the near-wall velocity profile of a streaming suspension with a resolution of tens of nanometers.[31] The near-wall dynamics of colloidal hard spheres dispersed in an organic solvent have been systematically studied over a broad range of volume fractions.[16,17] In the latest endeavor, experimental data were thoroughly compared with theoretical predictions based on a virial approximation and simulation results[32] where excellent agreement has been achieved.[18] This agreement between experiments and theory has provided a framework for the understanding of near-wall dynamics in general, and paved the way for the study of more complex systems.

Despite its high potential, EWDLS has not been employed to study the near-wall dynamics of particles in aqueous solution, except for very dilute suspensions. The main challenge is to find a suitable aqueous model system, which is monodisperse and can be refractive index-matched to the aqueous solvent to avoid multiple scattering. To this end, the fluorinated monomer 2,2,3,3,4,4,4-heptafluorobutyl methacrylate (FBMA) has been successfully used to synthesize monodisperse particles with a low refractive index *via* emulsion polymerization and the system was shown to form well-ordered crystalline colloidal arrays.[33] Further effort has led to the production of FBMA particles with radii between 50 nm to 700 nm.[34] However, such particles are susceptible to irreversible aggregation upon salt addition or under compression by centrifugation, as they are solely stabilized through electrostatic repulsion (ER) in aqueous solution. This would bring great difficulty into volume variation and interaction tuning, which is essential for the study of near-wall dynamics in dense suspensions. This situation calls for a more robust aqueous model system. The first attempt in this direction was made by Wiemann *et al.*, who designed a core–shell system with a fluoroacrylate core and a poly(ethylene glycol) (PEG) surface layer, for the study of glass transition and re-entry behaviour.[35] These so-called PEGylated particles are sterically stabilized in aqueous solution by the PEG layer, and were shown to be stable against compression up to a particle volume fraction of 69% and high salt concentrations. Continued effort has made it possible to synthesize particles with a single and well-defined PEG layer.[36] Moreover, this system bridges fundamental research to life science application, as PEG is a biocompatible material and *e.g.* PEGylation has already been widely used for drug delivery applications.[37,38]

In this paper we show that PEGylated FBMA particles are an interesting model system for the study of near-wall dynamics in aqueous solution for several reasons. First of all, they fulfill the requirements of being monodisperse, iso-refractive with aqueous solvents and stable, which ensures reliable EWDLS measurements; secondly, they are highly versatile, as their interactions can be tuned by varying the PEG chain length, the solvent composition, and salt concentrations where the PEG-layer should ensure colloidal stability even at high salt concentration. We describe the synthesis of the particles by emulsion polymerization and their bulk characterization, by cryo transmission electron microscopy (cryo-TEM) and light scattering. Finally we show that the near-wall dynamics of this model system is in very good agreement with current theoretical predictions for low particle volume fractions. However, due to the long range particle–particle interactions and those between the particles and the wall, the effect of increased concentration on the particles' near-wall dynamics is much more pronounced than for suspensions of colloidal hard spheres.

2 Experimental

2.1 Materials and synthesis

2.1.1 Materials. The fluorinated monomer 2,2,3,3,4,4,4-heptafluorobutyl methacrylate (HFBMA, 97%) was purchased from Alfa Aesar. Prior to use, the inhibitor hydroquinone was removed by washing the monomer three times with a 5% NaOH (w/v) solution. The macromonomer methoxy poly(ethylene glycol) acrylate with a molecular weight of M_n = 950 g mol^{-1} was purchased from Sigma-Aldrich. To remove the inhibitor from the PEG macromonomer, it was dissolved in water and passed through an inhibitor remover packed column (CAS, Sigma-Aldrich). Dimethylsulfoxide (DMSO) was purchased from Merck. The initiator, potassium peroxodisulfate ($K_2S_2O_8$), was obtained from Sigma-Aldrich.

2.1.2 Synthesis. The PEGylated fluorinated particles were prepared by surfactant free emulsion polymerization, following the procedure given in ref. 36. In a typical synthesis, 1000 mL H_2O are deoxygenated three times in a 3 L three-necked round bottom flask by firstly applying a vacuum and afterwards flooding with nitrogen. After deoxygenation, 34.9091 g (130 mmol) HFBMA and 69.7 mL of an acryl-PEG solution (10 g dissolved in 100 mL water; 6.97 g; 7.34 mmol) were added under inert gas countercurrent. The emulsion was heated to 70 °C under reflux cooling, and vigorous stirring (we used a magnetic stirrer bar which was driven by a motor with a nominal speed of 310 rpm). After 1 hour of homogenization the stirring speed is reduced to nominally 150 rpm and an adapter for a PTFE tube is added to the flask. A solution of 301 mg (1.1 mmol) $K_2S_2O_8$ in 10 mL H_2O is added with a syringe pump through the PTFE tube to the reaction mixture within 20 min.

After the injection is finished the reaction mixture turns turbid with a bluish colour. The input adapter is removed and the reaction is allowed to proceed for twenty hours. After cooling, the mixture is filtered through a Büchner funnel. To remove any remaining starting material, the dispersion is dialyzed for 7 days against deionized water from a Milli-Q water purification system with a resistivity of 18.2 MΩ cm^{-1}, changing the water twice a day. The solid content of the dialyzed dispersion was determined gravimetrically by drying three 1 mL aliquots at 100 °C under reduced pressure, weighing the solid remainder and calculating the average solid content.

2.2 Bulk characterization methods

2.2.1 Static and dynamic light scattering. The light-scattering measurements were performed on a commercial instrument by ALV-Laservertriebsgesellschaft (Langen, Germany) which is equipped with a HeNe Laser as a light source, an automated attenuator device, a Perkin Elmer avalanche diode and an ALV-6000 multiple tau digital correlator. Time-averaged static scattering intensities were obtained by measuring count rates of the diode and correcting them for attenuator transmission, scattering volume and solvent background. Furthermore, the scattering curves were normalized, using toluene as a reference and dividing out the particle concentration. Static intensities were recorded in an angular range between 30° and 120° with an increment of two degrees. Time auto correlation functions of the scattered intensity $g_2(Q,t)$ were recorded in a range of scattering angles $30° \leq \theta \leq 120°$ in steps of ten degree. Here $Q = 4\pi n_S \sin(\theta/2)/\lambda_0$ is the scattering vector with n_S the refractive index of the solution and λ_0 the vacuum wave length of the laser. To determine the diffusion constant of the particles, D_0, and their polydispersity index, U, a cumulant analysis of the correlation functions was performed. The particles' hydrodynamic radius, R_H, was calculated *via* the Stokes–Einstein relation, using the appropriate solvent viscosity.

2.2.2 Cryo transmission electron microscopy: cryo-TEM. Transmission cryo electron microscopy (cryo-TEM) was used to evaluate the morphology and size of the colloidal particles. 3 μL of a solution was applied on a hydrophilic Quantifoil TEM grid. In order to obtain a thin vitreous ice layer, the excess of solution was blotted for 2.5 seconds with a filter paper and the grid was plunged into liquid ethane in a FEI Vitrobot. The specimen was maintained at a temperature of approximately −196 °C using a cryo holder. Bright field TEM images were acquired on a FEI Spirit TEM operated at 120 kV. Since conventional TEM images correspond to two-dimensional (2D) projections of three-dimensional (3D) objects, electron tomography was performed to investigate the morphology of the colloidal particles. A series of 2D projections was acquired while tilting the specimen around an axis perpendicular to the electron beam over the range from −65° to 60° with an increment of 5°. After alignment, the 2D images were reconstructed by the Simultaneous Iterative Reconstruction Technique (SIRT) algorithm in the Astra Toolbox.[39]

2.3 Evanescent wave dynamic light scattering

2.3.1 EWDLS set-up. EWDLS experiments were performed with an instrument built in house, based on a triple axis diffractometer by Huber Diffraktionstechnik, Rimsting, Germany, which has been described in detail elsewhere.[15] The setup is equipped with a frequency doubled Nd/Yag Laser (Excelsior; Spectra Physics) with a vacuum wavelength of λ_0 = 532 nm and a nominal power output of 300 mW as a light source. Scattered light is collected with an optical enhancer system by ALV Lasververtriebsgesellschaft, Langen, Germany, and fed into two avalanche photo diodes by Perkin Elmer *via* an ALV fiber splitter. The TTL signals of the diodes are cross-correlated in time using an ALV-6000 multiple tau correlator. The scattering geometry and the definition of the scattering vector and its components parallel and normal to the interface are sketched in Fig. 1. The sample cell (custom-made by Hellma GmbH, Müllheim, Germany) consists of a hemispherical lens as the bottom part, made of SF10 glass, with an index of refraction n_1 = 1.736 at λ_0 = 532 nm. The suspension of FBMA particles is contained in a hemispherical dome which covers the lens from the top. The incident beam is reflected off the interface between the semi-spherical lens and the suspension, which is considered to be a flat wall. The resulting evanescent wave, which extends into the particle suspension is used as the illumination for the scattering experiment. It has a wave vector $\mathbf{k}_e$ pointing in the direction of the reflected beam's projection onto the reflecting interface. The scattering vector is given by $\mathbf{Q} = \mathbf{k}_s - \mathbf{k}_e$, where the scattered light wave vector, $\mathbf{k}_s$, is set by the two angles θ and α_r describing the position of the detecting unit.

The inverse penetration depth of the evanescent wave is determined by the angle of incidence α_i as $\kappa/2 = 2\pi\sqrt{(n_1 \sin\alpha_i)^2 - n_2^2}\,/\,\lambda_0$ and the refractive index of the glass n_1 and the suspension n_2, respectively. The magnitude of the scattering vector component parallel to the interface is given by $Q_\parallel = 2\pi n_2\sqrt{1 + \cos^2\alpha_r - 2\cos\theta\cos\alpha_r}\,/\,\lambda_0$ while the normal component is $Q_\perp = 2\pi n_2 \sin\alpha_r/\lambda_0$. The two components can be varied independently of each other by changing θ and α_r. To distinguish between particle dynamics parallel and normal to

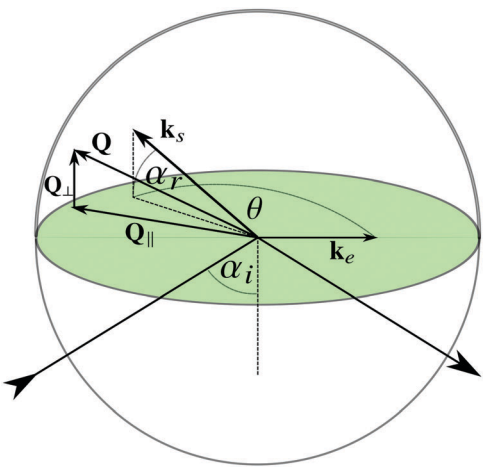

Fig. 1 Scattering geometry of an EWDLS experiment with spherical symmetry.

the wall, series of correlation functions are recorded at fixed $Q_\perp$ varying $Q_\parallel$ ($Q_\parallel$-scan) or *vice versa* ($Q_\perp$-scan).

2.3.2 EWDLS data analysis. The analysis of the scattered intensity time auto-correlation function $g_2(t)$ from EWDLS is more complicated than in conventional bulk dynamic light scattering (DLS), mainly for two reasons. The first major complication occurs from the fact that a simple quadratic Siegert relation between the measured $g_2(t)$ and the normalized correlation function of the scattered field $\hat{g}_1(t)$, which is usually assumed in DLS, does not apply in most cases in EWDLS. The scattering signal from the sample will be accompanied almost inevitably by a static scattering signal originating from surface corrugations, which can lead to large variations of the amplitude of the experimental correlation functions, as is shown in the top part of Fig. 2. Therefore, a mixed homodyne/heterodyne detection scheme has to be taken into account and a generalized Siegert relation[15]

$$g_2(t) = 1 + 2C_1\hat{g}_1(t) + (C_2\hat{g}_1(t))^2 \quad (1)$$

has to be applied for the conversion from $g_2(t)$ to $\hat{g}_1(t)$. Here, $C_2 = 1 - \sqrt{1-A}$ and $C_1 = C_2 - {C_2}^2$, with A the experimental intercept of $g_2(t)$.

Furthermore, in many cases EWDLS intensity-auto correlation functions exhibit a very slow decay at large times, as shown in the top part of Fig. 2. The physical origin of this slow relaxation is not clear yet. While Garnier *et al.* conjecture that it is due to a slow reversible adsorption of the particles to the wall due to van der Waals attraction,[11] Lisicki *et al.* argue that it is also caused by the unavoidable stray-light from surface defects, which is scattered by colloids in the bulk of the suspension into the detector.[40] Since these slow modes are in general well separated from the relaxation rates of interest, we approximate their contribution by an additional baseline B_1 to $\hat{g}_1(t)$.

Thus, to determine the initial slope Γ of $\hat{g}_1(t)$, which is related to the dynamic properties of interest, we chose to fit the experimental correlation functions, using a non-linear least squares algorithm, to eqn (1), where $\hat{g}_1(t)$ is modeled as a decaying single exponential function in time.

$$\hat{g}_1(t) = (1 - B_1)\exp\{-\Gamma t\} + B_1. \quad (2)$$

According to eqn (1) and (2), B_1 is related to B_2, the baseline of $g_2(t)$, by $B_1 = \sqrt{(C_1/C_2^2)^2 + B_2/C_2^2} - C_1/C_2^2$. Consequently there are three fit parameters A, Γ and B_2. Since an erroneous baseline value will lead to a deviation of Γ from the true relaxation rate, due to a normalization error, we fitted $g_2(t)$ repeatedly, starting with a number of data points, N_p. After the convergence of a single fit, two data points at the long time end of $g_2(t)$ were removed, and the remaining points were fitted again with reduced N_p. This procedure was repeated until $N_p < 20$. With this technique it was possible to identify a limited range of N_p's where the best fitting parameters are essentially independent of the number of points. The Γ values determined in this range are considered to be the initial slope or the first cumulant of $\hat{g}_1(t)$. Repeated measurements on the same sample show that Γ can be determined by this procedure with an uncertainty which is generally smaller than 10% as shown by the error bars displayed in Fig. 9.

2.3.3 Near-wall dynamics of particles with long range interactions. The mobility of colloids close to a wall is smaller than in bulk and depends on their distance, z from the wall due to the particles' hydrodynamic interaction with the wall. The resulting slowing down of Brownian motion is more pronounced in the direction normal to the wall than parallel to the wall. This has been described by two position dependent friction coefficients $\lambda_\parallel(z)$ and $\lambda_\perp(z)$.[24,25] In the simplest case of hard spherical particles the initial slope of the field correlation function Γ is related to these friction coefficients by

$$\Gamma = \langle D_\parallel \rangle_\kappa {Q_\parallel}^2 + \langle D_\perp \rangle_\kappa \left({Q_\perp}^2 + \frac{\kappa^2}{4} \right) \quad (3)$$

where $\langle D_{\parallel,\perp} \rangle_\kappa$ refer to position-dependent diffusion coefficients averaged over the illumination profile of the evanescent wave[14] as

$$\frac{\langle D_{\parallel,\perp} \rangle_\kappa}{D_0} = \kappa \int_R^\infty \mathrm{d}z \exp\{-\kappa(z-R)\}/\lambda_{\parallel,\perp}(z). \quad (4)$$

The superscript κ indicates that the averaged quantities depend slightly on the penetration depth of the evanescent wave.

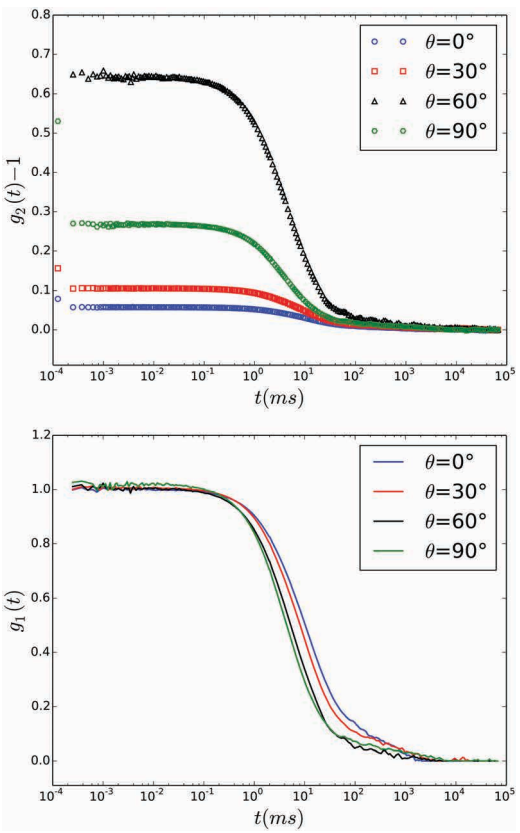

Fig. 2 Time auto correlation functions recorded during a $Q_\parallel$ scan in EWDLS at $\alpha_r = 60°$ and values of θ as indicated in the legend. Top: Intensity correlation functions $\hat{g}_2(t) - 1$ as measured. Bottom: Field correlation functions calculated by the generalized Siegert relation, eqn (1).

For particles, which are subject to a long-ranging interaction potential with the wall $V(z)$, the Boltzmann-factor of the potential will enter into the average diffusion constants[15] as

$$\frac{\langle D_{\parallel,\perp}\rangle_{\kappa}}{D_0} = \frac{\int_R^{\infty} \mathrm{d}z \exp\{-\beta V(z)\}\exp\{-\kappa(z)\}/\lambda_{\parallel,\perp}(z)}{\int_R^{\infty} \mathrm{d}z \exp\{-\beta V(z)\}\exp\{-\kappa(z)\}} \quad (5)$$

where $\beta = 1/k_{\mathrm{B}}T$ is the inverse thermal energy.

3 Results and discussion

3.1 Particle characterization

3.1.1 Synthesis and general properties. We prepared FBMA latex particles which are charge stabilized in aqueous media and which are additionally stabilized sterically by chemically attached PEG chains, according to a semi-batch emulsion polymerization procedure.[36] Electrophoresis measurements using a Malvern Zetasizer 2000, show that the particles behave as charged spheres at low ionic strengths with a zeta potential of −30 mV. The density of particles was determined to be 1.5266 g mL^{-1} with a density meter (Anton Paar DMA 4500). Given a particle radius of $R \approx 130$ nm (see section on cryo-TEM and bulk light scattering) this density results a sedimentation length $L_{\mathrm{s}} \approx 300R$, indicating that sedimentation should not significantly influence the results of the EWDLS experiments which were performed to investigate particle near-wall dynamics. This is experimentally verified by the typical standard deviations of repeated EWDLS measurements, as shown by the error bars in Fig. 9.

The particles yield turbid suspensions, if dispersed in water at volume fractions above $\phi \gtrsim 0.01$, since the refractive index of the fluorinated polymer is higher than that of water. In order to conduct light scattering measurement at higher concentrations, the refractive index of the particles needs to be matched to the surrounding medium by adding a co-solvent. DMSO was chosen as co-solvent because of its miscibility with water in all proportions, and its very low toxicity. A series of DMSO/water solutions was prepared, with refractive indices ranging from 1.33 to 1.40. To keep the particle concentration constant in all cases, 0.2 mL of a dialyzed stock suspension were added to 0.8 mL DMSO/water mixtures of various compositions. The scattering intensities of the resulting samples were measured at a scattering angle of $\theta = 90^{\circ}$, as the scattering intensity at constant volume fraction is approximately proportional to the square of the refractive index difference between the solvent and the particles. At a volume ratio of water to DMSO, $\phi(\mathrm{H_2O}):\phi(\mathrm{DMSO})$ of 69 : 31, the scattering intensity shows a minimum, which corresponds to the smallest obtainable refractive index difference between particles and solvent. The refractive index at this solvent composition was determined to be $n_{\mathrm{sol}} = 1.3847$, with an ABBEMAT RXA 156 refractometer from Anton Paar.

To obtain index-matched suspensions for further scattering experiments, the aqueous suspension was centrifuged at low speed and the sediments re-dispersed in the index-matching solvent mixture, for three times. The resulting dispersion is completely transparent and used as stock solution.

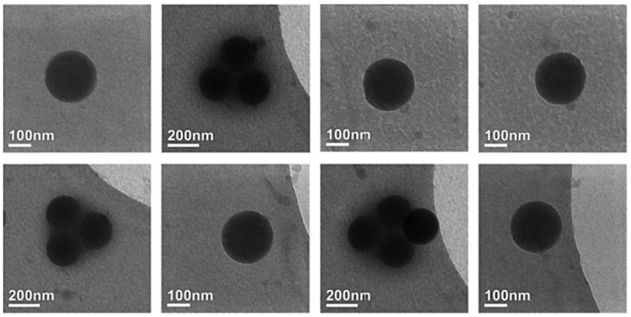

Fig. 3 Cryo-TEM images of single PEGylated FBMA particles and clusters.

3.1.2 Cryo-TEM. The shape and size of the particles were observed by cryo-TEM. In Fig. 3 we show representative images of single particles and some clusters which formed due to the blotting. The interfaces between the voids of the clusters and the spheres appear blurred, which we speculate might be due to the PEG chains. A total of 132 spheres were investigated to determine the mean particle radius and the relative standard deviation, which were found to be $R = 118$ nm and $\sigma_{\mathrm{r}} = 0.05$, respectively.

To confirm the spherical shape of the particles they were investigated by cryo-electron tomography. A series of 2D projections was acquired while tilting the specimen around an axis perpendicular to the electron beam (x-axis) over a range from −65° to +60° with a tilt increment of 5°. Example images from this series are shown in Fig. 4, where the perfectly circular shape of the 2D projection can be observed for all tilt angles. This observation is supported by the calculated 3D reconstruction which is displayed in Fig. 5.

The elongation of the 3D-reconstruction, which is observed in the zx and xy planes, is an artifact, which is caused by the limited number of acquisitions and the so-called missing wedge problem. The missing wedge is caused by the inability to tilt the sample over ±90° range. This is related to the limited gap between the pole pieces of the objective lens and shadowing effects of the TEM grid at high angles.[41] As the 3D reconstruction is

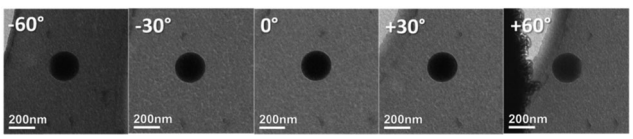

Fig. 4 2D projections of PEGylated FBMA particles as observed during a tomographic tilt series.

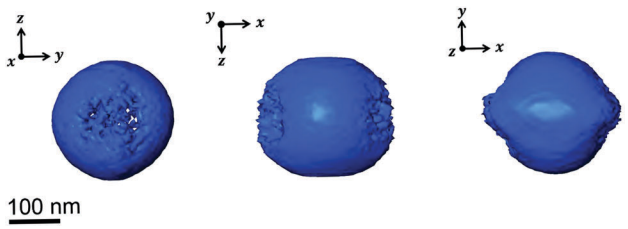

Fig. 5 Visualization of the 3D reconstruction. In the yz plane a spherical shape is observed, while in the zx and xy planes the reconstruction is elongated along the direction of the missing wedge.

mathematically speaking an ill-defined inverse problem, multiple solutions correspond to the incomplete data set that was collected. This eventually results in a blurring/elongation of the reconstruction in the direction of the missing wedge.

3.1.3 Static light scattering and phase behaviour. For a characterization of the particles in solution, combined static and dynamic light scattering experiments were performed. All the scattering data from bulk samples which will be discussed later were obtained from suspensions without any added salt. Therefore the salinity is about 10^{-5} mol L^{-1} due to carbon dioxide adsorption, corresponding to a Debye screening length of $l_D \approx 95$ nm. The time-averaged static scattering intensity, expressed in absolute intensities as the Rayleigh ratios $R(Q)$, from three samples with low volume fractions is shown in Fig. 6. The data obtained from the samples with different volume fractions, ϕ, in DMSO/water could be superimposed perfectly by dividing out the particle concentration, which indicates that at least up to $\phi = 0.014$ there is no discernible effect of the solution structure factor on the scattering curve. Intriguingly the shape of the scattering curve from the suspension in pure water differs significantly from the curves obtained from samples which were dispersed in the index-matching solvent. The latter two curves show a distinct minimum which could be misinterpreted to indicate a particle radius of about 200 nm. For homogeneous spheres the position of the first minimum in the particle form factor is related to the particle radius by $RQ_{min} \approx 4.49$. Thus for particles with a radius of about 120 nm, as indicated by cryo-TEM, the first minimum should occur at $Q_{min} \approx 0.037$ nm^{-1}, while here we find $Q_{min} \approx 0.023$ nm^{-1} implying a particle radius significantly larger than observed in cryo-TEM. This is a strong indication that the particles are not optically homogeneous spheres but rather exhibit a variation of the scattering contrast with distance from the particle centre.[42,43] We therefore fitted the static scattering data using the form factor of a core–shell particle with a core radius R_c and an outer radius R which is given by

$$P(Q) = \left\{ \frac{4\pi}{Q^3 V_\varepsilon} [\Delta\varepsilon_{cs}(\sin(QR_c) - QR_c\cos(QR_c)) + \Delta\varepsilon_{ss}(\sin(QR) - QR\cos(QR))] \right\}^2 \quad (6)$$

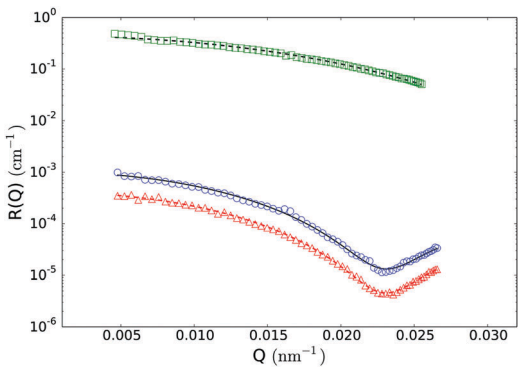

Fig. 6 Static light scattering data at low volume fractions. Open squares: $\phi = 5.6 \times 10^{-3}$ in water, open circles: $\phi = 1.4 \times 10^{-3}$ in DMSO/water, open triangles: $\phi = 5.6 \times 10^{-3}$ in DMSO/water, lines: best fits to data with eqn (7) resulting the parameters listed in Table 1.

where and $V_\varepsilon = 4\pi(\Delta\varepsilon_{cs}R_c^3 + \Delta\varepsilon_{ss}R^3)/3$ and $\Delta\varepsilon_{cs} = \varepsilon_c - \varepsilon_s$ is the difference between the dielectric constants of the core and the shell while $\Delta\varepsilon_{ss} = \varepsilon_s - \varepsilon_{sol}$ is the difference between the shell and the solvent with the corresponding refractive indexes $n_i = \sqrt{\varepsilon_i}$ of the core, the shell and the solvent respectively. To account for the particles' polydispersity we applied a logarithmic normal distribution $p(R_c)$ of the core radii assuming a constant shell thickness $d_{shell} = R - R_c$. With this the model function used for the fitting is

$$\Re(Q) = \frac{k_I^4}{16\pi^2}\phi\int_0^\infty p(R_c)V_p\left|\frac{\bar{\varepsilon} - \varepsilon_{sol}}{\varepsilon_{sol}}\right|^2 P(Q)\mathrm{d}R_c \quad (7)$$

with the wave vector of the incident beam, $k_I = 2\pi n_S/\lambda_0$, and the particles' average dielectric constant $\bar{\varepsilon} = (R_c^3\Delta\varepsilon_{cs} - R^3\varepsilon_s)/R^3$. The lines in Fig. 6 were obtained by simultaneously fitting the three sets of data with eqn (7), where the global parameters R_c, R, σ_r were forced to be the same for all three sets of data, while the local parameters n_c and n_s were allowed to vary between the data sets. The resulting best fitting parameter values are collected in Table 1.

The geometrical parameters are in very good agreement with the information deduced from cryo-TEM. Further we find $n_c \approx 1.38$ which is qualitatively in agreement the reported refractive index values for pure FBMA particles $n_{FBMA} \approx 1.37$.[34] The parameters associated with the particle shell are well in line with the picture of a thin PEG layer, which is swollen by the solvent. The molar mass of the PEG chain corresponds to an average degree of polymerization of $N \approx 22$, yielding an all-trans contour length of the chain $l_c \approx 8$ nm and a radius of gyration $R_g \approx 0.8$ nm if a length of about 0.13 nm per backbone atom[44,45] and a monomer segment length of approximately 0.38 nm is assumed. This implies that a shell consisting of PEG should have a thickness between approximately 1.5 nm and 8 nm in accordance with our findings from SLS $\langle R\rangle - \langle R_c\rangle = 5.9$ nm. Assuming an ideal mixture, we can obtain an estimate for the PEG volume fraction in the shell as $\phi_{PEG} = (n_s - n_{sol})/(n_{PEG} - n_{sol})$. Applying $n_{PEG} \approx 1.358$[46] this yields a polymer volume fraction of about 20% in both solvents. These findings strongly indicate that our particles exhibit a pronounced core shell structure with a significant enrichment of the PEG chains at the surface of an FBMA core, which was not reported before.

Generally, with increasing volume fraction of the particle suspension, a transition from an isotropic solution to a colloidal crystal is expected. Indeed, FBMA-particle suspensions with volume fractions $\phi > 10$ are opalescent, indicating the formation of an

Table 1 Best fitting parameter values obtained from fitting the static light scattering data to eqn (7)

Solvent volume fraction	H_2O 0.0056	H_2O/DMSO 0.0056	H_2O/DMSO 0.014
$\langle R_c\rangle$/nm	115.3	115.3	115.3
$\langle R\rangle$/nm	121.2	121.2	121.2
σ_r	0.08	0.08	0.08
n_c	1.3838	1.3839	1.3839
n_s	1.3549	1.400	1.3999

ordered structure. With lower volume fractions this colourful effect vanishes gradually and the determination of the transition volume fraction by optical inspection is rather ambiguous. Therefore we applied the Hansen–Verlet criterion to estimate the lowest volume fraction at which coexistence between an isotropic solution and an ordered structure occurs. According to this empirical rule, it is generally accepted that the maximum of the structure factor $S(Q_{max}) = 2.85$ at the freezing point of colloidal hard sphere suspensions,[47] while it slightly increases for particles interacting by electrostatic repulsion (ER), depending weakly on their surface charge density and the solvent salinity. For charged particles at low salinity, as in our case the threshold value is $S(Q_{max}) \approx 3.0$–3.1.[48–51] In Fig. 7 we plotted the structure factors of suspensions with different volume fractions, obtained from the static scatting data according to

$$S(Q) \approx \frac{I(Q,\phi)}{I(Q,\phi_0)}\frac{\phi_0}{\phi} \quad (8)$$

where $I(Q,\phi_0)$ was measured at $\phi_0 = 1.4 \times 10^{-2}$ at which the structure factor is unity at all Q to a very good approximation.

At the given salinity $S(Q_{max}) \lesssim 3$ for the sample with $\phi = 0.07$, while the structure factor maximum is significantly larger than the threshold value for the sample with 8% volume fraction. Thus, at $\phi = 0.08$ there is definitely a coexistence between an isotropic solution and an ordered structure.

3.1.4 Dynamic light scattering. Before conducting experiments on near-wall dynamics, it is important to check if and how the index-matching solvent influences the diffusion behaviour of the system in bulk other than by viscous friction. For this purpose, we performed dynamic light scattering experiments on dilute particle dispersions both in water and in the index-matching DMSO/water mixture. Fig. 8 shows a plot of the first cumulant Γ_1 *vs.* Q^2 for particles dispersed in pure water and in the mixed solvent, respectively. The diffusion coefficient of the particles is the slope of the observed linear relations, $D_0 = 1630$ nm^2 ms^{-1} in water and 746 nm^2 ms^{-1} in the mixed solvent. The hydrodynamic radius, calculated through the Stokes–Einstein relation is $R_H = 131$ nm in both cases, when

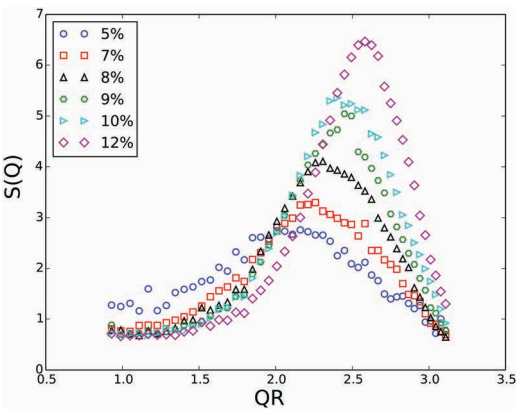

Fig. 7 Structure factors obtained from PEGylated FBMA particle suspensions in index-matching DMSO/water mixtures with different volume fractions as indicated in the legend and a screening length of $l_D \approx 95$ nm.

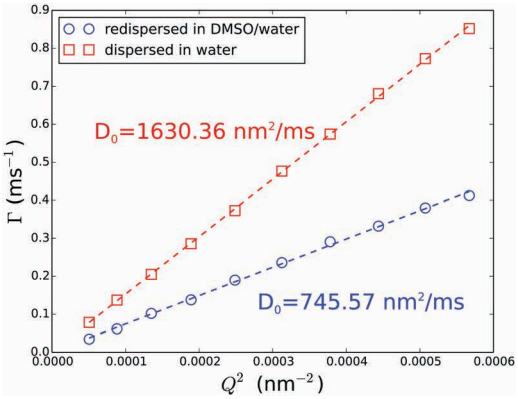

Fig. 8 Bulk DLS result of PEGylated FBMA particles dispersed in water (open red squares) and in DMSO/water mixture (open blue circles). Symbols represent experimental data and lines are linear least squares fits with slopes equal to the diffusion coefficients, D_0, as indicated.

the correct values for the solvent viscosity are used, *i.e.* $\eta = 1$ mPa s for water and 2.187 mPa s for the mixed solvent. This shows that the solvent exchange has no effect on the particles' bulk dynamic except for the increased viscous friction. Moreover, the linearity of Γ_1 *versus* Q^2 plots in both cases is a first hint to a narrow particle size distribution indicating the absence of aggregates in the dispersions. A more thorough estimate of the particle size distribution can be obtained from a cumulant analysis of the correlation functions. The polydispersity index is given by $U = \Gamma_2/\Gamma_1^2$ where Γ_2 is the second cumulant. We find $U = 0.03$ for the particles in pure water and 0.09 in the solvent mixture. Assuming a logarithmic normal distribution of the particle radii these figures correspond to a relative standard deviation $\sigma_r \approx 0.05$ in the first case, which is in perfect agreement with the observed standard deviation from cryo-TEM. The relative standard deviation measured in the index-matching solvent mixture is 0.1 again showing there is no significant aggregation of particles in this case. The hydrodynamic radius obtained from DLS is larger than the geometric radius obtained from cryo-TEM, which is $R = 120$ nm. This is explained by the fact that the two methods measure different moments of the size distribution. For a logarithmic normal distribution the ratio of both quantities is related to the standard deviation by $R_H/R = (1 + \sigma^2)^5$ which for the present system implies a relative standard deviation of the order of ten percent in good agreement with the values from the cumulant analysis of DLS data.

3.2 EWDLS measurements

To investigate the PEGylated FBMA particles near-wall dynamics at low volume fractions, we performed EWDLS measurements on suspensions with $\phi = 0.01$. As the colloids and the glass surface are negatively charged, the addition of electrolyte will make a difference to the particles' near-wall dynamics, by changing the range of the electrostatic repulsion (ER). To illustrate this influence, Fig. 9 shows values of Γ plotted *versus* the square of the parallel scattering vector component obtained during parallel scans, at two different salt concentrations. Here and in the following we show normalized quantities, where $d = 2R_H$ is the

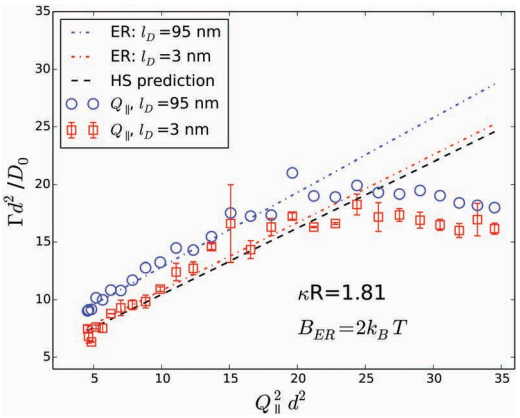

Fig. 9 Normalized initial relaxation rates Γ as a function of the parallel scattering vector component squared. Symbols represent experimental data obtained from a ϕ = 0.01 sample at different Debye screening lengths, as indicated in the legend. Lines represent theoretical predictions for infinite dilution according to eqn (5) and (9). The error bars assigned to the data obtained from the sample with added salt, represent standard deviations from three repeated measurements.

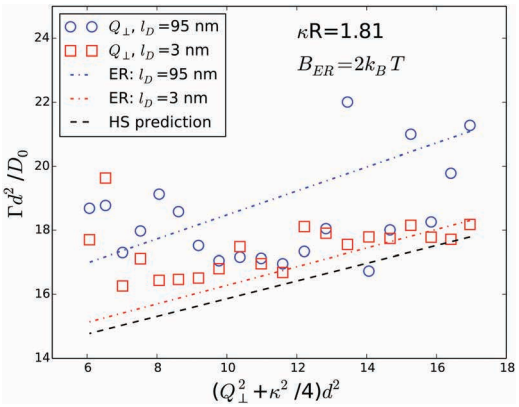

Fig. 10 Normalized initial relaxation rates Γ as a function of the normal scattering vector component squared. Symbols represent experimental data obtained from a ϕ = 0.01 sample at different Debye screening lengths, as indicated in the legend. Lines represent theoretical predictions for infinite dilution according to eqn (5) and (9).

particle diameter, to facilitate comparison between the results obtained from different systems, in particular with a hard sphere system as shown in Fig. 12. The red symbols represent a sample with 10 mM NaCl, which corresponds to a Debye length of l_D = 3 nm. In this situation the electrostatic repulsion (ER) is almost completely screened and the measured Γ agree within experimental error with the prediction for a hard sphere with a hydrodynamic radius of R_H = 130 nm, represented by the black line in Fig. 9. The error bars assigned to these data, which represent the standard deviation of three repeated measurements, are representative for all EWDLS data discussed in the following. For the sake of clarity we will not display error bars in the following graphs. The data represented by the blue symbols were obtained from the sample without extra salt addition, which corresponds to an ionic strength $\sim 10^{-5}$ M and a Debye length of l_D = 95 nm. In this suspension, the particles move significantly faster than those dispersed at a high salt concentration. This can be explained intuitively, since the long range electrostatic repulsion (ER) will effectively push the particles away from the interface thereby reducing the hydrodynamic wall drag effect. To quantitatively analyze these data, we calculated the Γ *vs.* $Q_\parallel{}^2$ dependence, by numerically integrating eqn (5) into which we introduced the electrostatic interaction potential which may be approximated within the Debye–Hückel–Derjaguin limit by

$$V_{es}(z) = B_{ER}\exp\{-(z - R)/l_D\} \quad (9)$$

The amplitude B_{ER} scales with particle radius and depends on the surface charge density of particles and the wall. In the model calculations, this amplitude is the only adjustable parameter and we could achieve good agreement between all experimental data discussed in this paper and the predictions with a fixed value of $B_{ER} = 2k_BT$. In Fig. 9 and 10, the lines labeled ER represent predictions for l_D = 95 nm (blue), and for l_D = 3 nm (red). The black line shows the hard sphere prediction as a reference, where no electrostatic interaction is taken into account. The systematic deviation of the experimental data at high $Q_\parallel$ is due to the fact that the primary laser beam is reflected upon exiting of the semi-spherical lens, by that giving rise to a second scattering event with an in-plane angle $\theta_r = 180 - \theta$. This effect is frequently observed, even in bulk experiments, with index-matched particles. For the case of EWDLS on hard sphere samples it has been discussed in detail in a previous paper.[18] As a consequence of this back reflection, data obtained from EWDLS experiments at $\theta > 90°$ are often not reliable, which in the present case corresponds to $(Q_\parallel d)^2 \gtrsim 30$, given $\alpha_r = 60°$ and the refractive index of the solution $n_S \approx 1.38$.

The agreement between experiments and predictions is less satisfying in the case of the $Q_\perp$-scans, as shown in Fig. 10, since the scatter of the experimental data is significantly larger, especially at long Debye lengths. At high salt concentrations the experimental data are reasonably well represented by the prediction for a Debye length of 3 nm, while the experimental data obtained from the sample without additional salt follow the prediction only qualitatively.

To investigate the influence of the evanescent wave penetration depth on the measured values of Γ we performed experiments at different angles of incidence. Fig. 11 shows data obtained from $Q_\parallel$-scans at two different penetration depths together with the corresponding theoretical prediction. Although the agreement is very good, the scatter of the experimental data is larger than the difference between the predictions for different penetration depths. Thus, the influence of the penetration depth is too small to be reliably detected experimentally.

So far, we have shown that in dilute suspensions, PEGylated FBMA particles behave like charged spheres, and their near-wall dynamics can be suitably described by a combination of hydrodynamic wall effect and the particles' static interaction with the wall. However, a more interesting and challenging question concerns the near-wall dynamics at increased volume fractions, at which the system changes from an isotropic solution to an ordered structure, stabilized by long-ranged particle

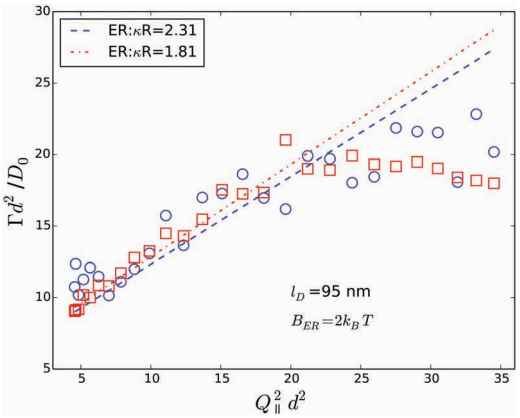

Fig. 11 Effect of evanescent wave penetration depth on measured Γ. Symbols represent experimental data obtained from a ϕ = 0.01 sample at different penetration depths. Lines of equal color represent theoretical predictions for infinite dilution according to eqn (5) and (9). Penetration depths are indicated in the legend.

interactions. As a first step to tackle this question we show data obtained from a suspension with a particle volume fraction of 7% in Fig. 12. The graph displays the normalized Γ *versus* $Q_\parallel{}^2$ data, obtained at κR = 1.81 from a suspension without added salt. As a general trend we observe that the relaxation rates are lager at ϕ = 0.07 than at infinite dilution, which is represented by the dashed dotted line. Further, there is a significant deviation from the linear $Q_\parallel{}^2$ behaviour, which was observed at low volume fraction. The relaxation rates rather undulate with $Q_\parallel{}^2$ which is very reminiscent of the behaviour we reported earlier for hard spheres at high volume fractions. For comparison we also show experimental data obtained from a suspension of hard spheres at a volume fraction of 30% together with a set of simulated data for the same system. Note that these data were obtained at $\alpha_r = 27.8^\circ$ and $n_S \approx 1.49$, thus the effect of back reflections will only become visible at $(Q_\parallel d)^2 \gtrsim 50$. Based on the observed qualitative similarity we conjecture that also the near-wall dynamics of the PEGylated FBMA particles at ϕ = 0.07 are significantly affected by the suspension's structure factor, which is in line with our observation that suspensions with a volume fraction of 7% are close to the disorder/order coexistence of the system. A systematic experimental investigation and a quantitative theoretical analysis of this effect will be the subject of a future contribution.

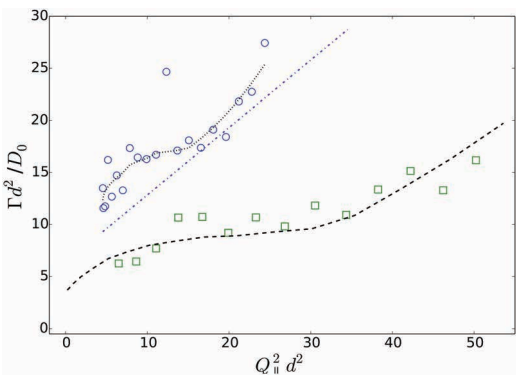

Fig. 12 Comparison of $Q_\parallel$-scans on a PEGylated FBMA suspension with ϕ = 0.07 (open circles) and a hard sphere system at ϕ = 0.3 (open squares). The dashed line represents simulation data for the hard sphere system, the dashed dotted line is the prediction for charged spheres at low ϕ according to eqn (5) and (9) and the dotted line is a guide for the eyes.

4 Conclusion

We have synthesized PEGylated fluorinated particles by an emulsion polymerization, for the study of near-wall dynamics of colloidal particles in aqueous solution. Bulk characterizations show that the particles have a core shell structure, a negligible polydispersity, are stable against compression and addition of salt, and can be easily index-matched to aqueous solutions, which makes them a good model system for scattering experiments in aqueous suspensions at increased concentrations up to the transition from an isotropic solution to an ordered phase and beyond. By static light scattering we have shown that a coexistence of isotropic and ordered suspensions already occurs at a volume fraction of 8% in DMSO/water, if no additional electrolyte is present. In future we will use this system for the systematic investigation of near-wall dynamics of particles with long-ranging interactions. In this contribution we showed that EWLDS measurements on this system produce reliable and reproducible data. At low volume fractions the near-wall dynamics can be well predicted taking into account the particles hydrodynamic and electrostatic interaction with the wall. However, even at moderate volume fractions the near-wall dynamics are reminiscent of the behaviour which was observed for hard spheres at much higher volume fractions, which is attributed to the long range particle–particle repulsion. A thorough experimental investigation of the interaction effects on near-wall dynamics and the design of a theoretical framework for their prediction is the objective of ongoing work.

Acknowledgements

The authors thank Prof. J. K. G. Dhont and the ICS-3 group for useful discussions and support. YL would like to thank the Marie Sklodowska Curie Initial Training Network SOMATAI under the EU Grant Agreement No. 316866 for financial support. BT contributed to this work during an internship at Forschungszentrum Jülich supported by the International Helmholtz Research School of Biophysics and Soft Matter (IHRS BioSoft), which is gratefully acknowledged. SB and NC acknowledge financial support from the European Research Council (ERC Starting Grant No. 335078-COLOURATOMS).

References

1 *Soft Matter at Aqueous Interfaces*, ed. P. R. Lang and Y. Liu, Springer, Doordrecht, 2016, pp. 1–556.
2 *Particle-Stabilized Emulsions and Colloids*, ed. T. Ngai and S. Bon, The Royal Society of Chemistry, 2015, pp. P001–P322.

3 J. D. Andrade and V. Hlady, Protein adsorption and materials biocompatibility: a tutorial review and suggested hypotheses, *Biopolymers/Non-Exclusion HPLC*, Springer Berlin Heidelberg, Berlin, Heidelberg, 1986, pp. 1–63.
4 L. Hu, M. Chen, X. Fang and L. Wu, *Chem. Soc. Rev.*, 2012, **41**, 1350–1362.
5 M. Zheludkevich, J. Tedim and M. Ferreira, *Electrochim. Acta*, 2012, **82**, 314–323.
6 I. W. Cheong and J. H. Kim, *Chem. Commun.*, 2004, 2484–2485.
7 D. T. Wasan and A. D. Nikolov, *Nature*, 2003, **423**, 156–159.
8 D. T. Wasan, A. D. Nikolov, A. Trokhymchuck and D. J. Henderson, Confinement-Induced Structural Forces in Colloidal Systems, in *Encycopedia of Surface and Colloidal Science*, ed. P. Somasundaran, CRC Press Taylor and Francis, Boca Raton, FL, 2006, p. 1485.
9 H. Löwen, *J. Phys.: Condens. Matter*, 2009, **21**, 474203.
10 M. I. M. Feitosa and O. M. Mesquita, *Phys. Rev. A: At., Mol., Opt. Phys.*, 1991, **44**, 6677–6685.
11 N. Garnier and N. Ostrowsky, *J. Phys. II*, 1991, **1**, 1221–1232.
12 M. Hosoda, K. Sakai and K. Takagi, *Phys. Rev. E: Stat. Phys., Plasmas, Fluids, Relat. Interdiscip. Top.*, 1998, **58**, 6275–6280.
13 B. Lin, J. Yu and S. A. Rice, *Phys. Rev. E: Stat. Phys., Plasmas, Fluids, Relat. Interdiscip. Top.*, 2000, **62**, 3909–3919.
14 P. Holmqvist, J. K. G. Dhont and P. R. Lang, *Phys. Rev. E: Stat., Nonlinear, Soft Matter Phys.*, 2006, **74**, 021402.
15 P. Holmqvist, J. K. G. Dhont and P. R. Lang, *J. Chem. Phys.*, 2007, **126**, 044707.
16 V. Michailidou, G. Petekidis, J. Swan and J. Brady, *Phys. Rev. Lett.*, 2009, **102**, 068302.
17 V. N. Michailidou, J. W. Swan, J. F. Brady and G. Petekidis, *J. Chem. Phys.*, 2013, **139**, 164905.
18 Y. Liu, J. Bławzdziewicz, B. Cichocki, J. K. G. Dhont, M. Lisicki, E. Wajnryb, Y.-N. Young and P. R. Lang, *Soft Matter*, 2015, **11**, 7316–7327.
19 P. Mathai, Brownian Motion in Microfluidics and Nanofluidics, in *Encyclopedia of Microfluidics and Nanofluidics*, ed. D. Li, Springer New York, New York, NY, 2015, pp. 213–218.
20 D. M. Kaz, R. McGorty, M. Mani, M. P. Brenner and V. N. Manoharan, *Nat. Mater.*, 2011, **11**, 138–142.
21 E. M. Herzig, K. A. White, A. B. Schofield, W. C. K. Poon and P. S. Clegg, *Nat. Mater.*, 2007, **6**, 966–971.
22 M. L. Gibiansky, J. C. Conrad, F. Jin, V. D. Gordon, D. A. Motto, M. A. Mathewson, W. G. Stopka, D. C. Zelasko, J. D. Shrout and G. C. L. Wong, *Science*, 2010, **330**, 197.
23 I. H. Riedel, K. Kruse and J. Howard, *Science*, 2005, **309**, 300–303.
24 H. Brenner, *Chem. Eng. Sci.*, 1961, **16**, 242–251.
25 A. Goldman, R. Cox and H. Brenner, *Chem. Eng. Sci.*, 1967, **22**, 653–660.
26 S. Das, A. Garg, A. I. Campbell, J. R. Howse, A. Sen, D. Velegol, R. Golestanian and S. J. Ebbens, *Nat. Commun.*, 2015, **6**, 8999.
27 J. Elgeti, R. G. Winkler and G. Gompper, *Rep. Prog. Phys.*, 2015, **78**, 056601.
28 K. H. Lan, N. Ostrowsky and D. Sornette, *Phys. Rev. Lett.*, 1986, **57**, 17–20.
29 S. A. Rogers, M. Lisicki, B. Cichocki, J. K. G. Dhont and P. R. Lang, *Phys. Rev. Lett.*, 2012, **109**, 098305.
30 A. Stocco, T. Mokhtari, G. Haseloff, A. Erbe and R. Sigel, *Phys. Rev. E: Stat., Nonlinear, Soft Matter Phys.*, 2011, **83**, 011601.
31 B. Loppinet, J. K. G. Dhont and P. Lang, *Eur. Phys. J. E: Soft Matter Biol. Phys.*, 2012, **35**, 1–4.
32 B. Cichocki, E. Wajnryb, J. Blawzdziewicz, J. K. G. Dhont and P. R. Lang, *J. Chem. Phys.*, 2010, **132**, 074704.
33 G. Pan, A. S. Tse, R. Kesavamoorthy and S. A. Asher, *J. Am. Chem. Soc.*, 1998, **120**, 6518–6524.
34 G. H. Koenderink, S. Sacanna, C. Pathmamanoharan, M. Rasa and A. P. Philipse, *Langmuir*, 2001, **17**, 6086–6093.
35 M. Wiemann, R. Schneider and E. Bartsch, *Z. Phys. Chem.*, 2012, **226**, 761–778.
36 J. Ulama, M. Zackrisson Oskolkova and J. Bergenholtz, *J. Phys. Chem. B*, 2014, **118**, 2582–2588.
37 M. Z. Oskolkova, A. Stradner, J. Ulama and J. Bergenholtz, *RSC Adv.*, 2015, **5**, 25149–25155.
38 D. Pozzi, V. Colapicchioni, G. Caracciolo, S. Piovesana, A. L. Capriotti, S. Palchetti, S. De Grossi, A. Riccioli, H. Amenitsch and A. Laganà, *Nanoscale*, 2014, **6**, 2782–2792.
39 W. Van Aarle, W. J. Palenstijn, J. De Beenhouwer, T. Altantzis, S. Bals, K. J. Batenburg and J. Sijbers, *Ultramicroscopy*, 2015, **157**, 35–47.
40 M. Lisicki, B. Cichocki, J. K. G. Dhont and P. R. Lang, *J. Chem. Phys.*, 2012, **136**, 204704.
41 P. A. Midgley and M. Weyland, *Ultramicroscopy*, 2003, **96**, 423–431.
42 P. Schurtenberger, Contrast and contrast variation in neutron, X-ray, and light scattering, in *Neutrons, X-rays and Light: Scattering Methods Applied to Soft Condensed Matter*, ed. L. Peter and T. Zemb, North-Holland, Amsterdam, 2002, p. 145.
43 M. Zackrisson, A. Stradner, P. Schurtenberger and J. Bergenholtz, *Langmuir*, 2005, **21**, 10835–10845.
44 C. Tanford, *The Hydrophobic Effect*, Wiley, New York, 1973.
45 J. Israelachvili, *Intramolecular and Surface Forces*, Academic Press, 2nd edn, 1991, p. 370.
46 S. Ottani, D. Vitalini, F. Comelli and C. Castellari, *J. Chem. Eng. Data*, 2002, **47**, 1197–1204.
47 J. P. Hansen and L. Verlet, *Phys. Rev.*, 1969, **184**, 151.
48 H. S. Kang and F. H. Ree, *J. Chem. Phys.*, 1995, **103**, 3629.
49 D. C. Wang and A. P. Gast, *J. Phys.: Condens. Matter*, 1999, **11**, 10133–10141.
50 J. Gapinski, G. Nägele and A. Patkowski, *J. Chem. Phys.*, 2012, **136**, 024507.
51 J. Gapinski, G. Nägele and A. Patkowski, *J. Chem. Phys.*, 2014, **141**, 124505.